Magnetic Resonance in Medicine

Improved repeatability of dynamic contrast-enhanced MRI using the complex MRI signal to derive arterial input functions: a test-retest study in prostate cancer patients

Edzo M.E. Klawer[1] 🆔 | Petra J. van Houdt[1] 🆔 | Frank F.J. Simonis[2] 🆔 |
Cornelis A.T. van den Berg[2] 🆔 | Floris J. Pos[1] | Stijn W.T.P.J. Heijmink[3] |
Sofie Isebaert[4] | Karin Haustermans[4] | Uulke A. van der Heide[1] 🆔

[1]Department of Radiation Oncology, the Netherlands Cancer Institute, Amsterdam, The Netherlands

[2]Department of Radiation Oncology, Imaging Division, University Medical Center, Utrecht, The Netherlands

[3]Department of Radiology, the Netherlands Cancer Institute, Amsterdam, The Netherlands

[4]Department of Radiation Oncology, Leuven Cancer Institute, University Hospitals Leuven, Leuven, Belgium

Correspondence
Uulke A. van der Heide, Department of Radiation Oncology, The Netherlands Cancer Institute, Plesmanlaan 121, 1066 CX Amsterdam, The Netherlands.
Email: u.vd.heide@nki.nl

Purpose: The arterial input function (AIF) is a major source of uncertainty in tracer kinetic (TK) analysis of dynamic contrast-enhanced (DCE)-MRI data. The aim of this study was to investigate the repeatability of AIFs extracted from the complex signal and of the resulting TK parameters in prostate cancer patients.

Methods: Twenty-two patients with biopsy-proven prostate cancer underwent a 3T MRI exam twice. DCE-MRI data were acquired with a 3D spoiled gradient echo sequence. AIFs were extracted from the magnitude of the signal (AIF_{MAGN}), phase (AIF_{PHASE}), and complex signal ($AIF_{COMPLEX}$). The Tofts model was applied to extract K^{trans}, k_{ep} and v_e. Repeatability of AIF curve characteristics and TK parameters was assessed with the within-subject coefficient of variation (wCV).

Results: The wCV for peak height and full width at half maximum for $AIF_{COMPLEX}$ (7% and 8%) indicated an improved repeatability compared to AIF_{MAGN} (12% and 12%) and AIF_{PHASE} (12% and 7%). This translated in lower wCV values for K^{trans} (11%) with $AIF_{COMPLEX}$ in comparison to AIF_{MAGN} (24%) and AIF_{PHASE} (15%). For k_{ep}, the wCV was 16% with AIF_{MAGN}, 13% with AIF_{PHASE}, and 13% with $AIF_{COMPLEX}$.

Conclusion: Repeatability of AIF_{PHASE} and $AIF_{COMPLEX}$ is higher than for AIF_{MAGN}, resulting in a better repeatability of TK parameters. Thus, use of either AIF_{PHASE} or $AIF_{COMPLEX}$ improves the robustness of quantitative analysis of DCE-MRI in prostate cancer.

KEYWORDS
arterial input function, complex signal, dynamic contrast-enhanced MRI, prostate cancer, repeatability, tracer kinetic analysis

1 | INTRODUCTION

Dynamic contrast-enhanced (DCE)-MRI is a valuable method to characterize cancer, given that many tumors show distinctive enhancement patterns. This could provide promising information for prognosis and treatment response monitoring.[1,2] In order to quantify the perfusion and permeability of the tissue microvasculature, tracer kinetic (TK) analysis can be applied. The Tofts model[3] provides the parameters K^{trans} and k_{ep}, representing the transfer constant of contrast agent (CA) from blood plasma to the extravascular extracellular space in tissue (K^{trans}) and the rate constant from the extravascular extracellular space back into the blood plasma (k_{ep}). However, large variations occur in values of the TK parameters between DCE-MRI examinations of different studies and institutions.[4-6] These variations are related to the complexity[7] and variety of choices that are possible in both the acquisition and analysis of DCE-MRI data.[8] Even within a single institution, variations in TK parameters as high as 74% have been reported.[5] The lack of repeatability severely limits the possibility of finding treatment-related changes.

One of the main contributors to variations in TK parameters is the arterial input function (AIF).[9,10] The AIF represents the absolute CA concentration in a feeding artery as a function of time. However, measurement of the AIF with MRI is prone to artifacts. When it is not possible to acquire individualized (patient-specific) AIFs, population-based AIFs are a good alternative as proposed by Parker et al.[11] However, in such cases, patient-intrinsic differences will be ignored. Port et al showed that the peak enhancement and area under the curve (AUC) between individual AIFs can vary up to a factor of 2.5 and 3.7, respectively, between patients.[12] Rijpkema et al reported that incorporating these differences between the individualized AIFs into the TK results in a substantial reduction in variation between patient measurements.[13] Therefore, despite the difficulty of measuring the AIF accurately, use of individualized AIFs is still preferred.

Usually, the AIF is extracted from the magnitude of the MRI signal. However, in spoiled gradient echo (SPGR) sequences, the magnitude of the signal is sensitive to saturation at higher concentrations, depending on acquisition parameters, causing an underestimation of the peak height of the AIF.[14] This results in an overestimation of K^{trans}. In addition, the magnitude signal is sensitive for inflow effects and inhomogeneity of the B_1 field.[15,16] Sequences can be developed that minimize these effects, for example, by increasing flip angle and increasing the field of view (FOV) in the feet-head direction. However, particularly at 3T, this comes at the cost of a lower spatial or temporal resolution to limit the specific absorption rate (SAR). An alternative is to extract the AIF from the phase of the signal.[4,15] This is attractive given that the phase has a linear relation to the CA concentration and is not sensitive to B_1 inhomogeneity and inflow effects. However, phase measurements are noisy, particularly at low CA concentrations, and can suffer from phase drift.[17] A promising way to deal with these problems is to use the complex signal. This method was first introduced by Van Osch et al with the aim to reduce partial volume effects in case of low spatial resolution dynamic susceptibility-contrast MRI[18] and DCE-MRI.[19] Simonis et al applied this method to AIF estimation in DCE-MRI measurements in patients with prostate cancer.[20] To fully exploit the information content of the complex data, they reformulated the signal-to-concentration model allowing joint estimation of concentration time curve, baseline signal level, and effective B_1 correction from 1 minimization over all time points. In this way, the complementary strengths of the magnitude and phase methods are used, giving it a high precision and accuracy over the complete range of in vivo occurring concentrations. In their study, they demonstrated the improvement of the AIF compared to AIFs derived from magnitude or phase alone. Moreover, they demonstrated consistency between the AIF and TK parameters obtained from DCE-MRI with those obtained from DCE-CT (computed tomography) measurements.

Given that a high repeatability of DCE-MRI measurements is essential for treatment-monitoring applications, the aim of this study is to investigate the repeatability of both the AIF extracted from the complex signal and the subsequently derived TK parameters in patients with prostate cancer. The results will be compared to the AIFs and TK parameters derived from the magnitude signal and phase signal.

2 | METHODS

2.1 | Patient inclusion

Twenty-two patients with biopsy-proven prostate cancer (median age, 68 years; range, 54–76) from 2 different institutes (the Netherlands Cancer Institute [n = 15] and University Hospitals Leuven [n = 7]) underwent a multiparametric (mp)-MRI exam twice, before prostatectomy. The median time interval between the 2 exams was 17 days (range, 3–37). No interventions took place between the 2 consecutive exams. The median time between biopsy and first MR examination was 5 weeks (range, 4–140). The median time between the first examination and the prostatectomy was 5 weeks (range, 1–13). The study was approved by the local ethics board. Patients were included between October 2014 and March 2016. The local ethics review boards approved this study, and all patients gave written informed consent for their participation.

2.2 | Imaging protocol

Patients were scanned on 3 different scanners from the same vendor (Philips Healthcare, Best, The Netherlands): System

I was a 3T Achieva using a cardiac and endorectal coil (n = 12), system II was a 3T Achieva dStream with an anterior-posterior coil (n = 3), and system III was a 3T Ingenia with an anterior-posterior coil (n = 7). The mp-MRI exam consisted of a T2-weighted MRI, diffusion-weighted MRI (DWI), and a DCE-MRI scan. The first 2 were used for delineation of the tumor and registration purposes. Details of the scan parameters are summarized in Table 1. The DCE-MRI scans were acquired with a 3D SPGR sequence. After the second dynamic scan, 7.5 mL of gadoteric acid (15 mL of 0.5 M of Dotarem; Guerbet, Roissy CdG, France) was injected, followed by a 30-mL saline flush, using a power injector. Because it takes time for the bolus to arrive in the FOV, the first 10 dynamic scans could be used to determine the baseline. To convert intensities of DCE-MRI data into concentration values, a precontrast T1-map was generated, using a variable flip angle series acquired with a 3D SPGR sequence (TR/TE, 20.0 ms/4.0 ms) with flip angles of 3, 6, 10, 20, and 30°.[14] To compensate for B_1-inhomogeneity, a B_1 map was acquired in each exam using the dual-TR method[21] and resampled to the reconstructed voxel size of the DCE-MRI acquisition.

2.3 | AIF measurement

To extract the AIF, regions of interest (ROIs) in the left and right femoral arteries were manually delineated using the dynamic scan with maximum contrast between the arteries and surrounding tissue. To obtain optimal AIFs from magnitude and phase data, a minimum of 4 slices were used where the 3 most cranial and 3 most caudal slices of the stack were not used, to reduce inflow artifacts and slice profile effects. Slices at the bifurcations were avoided for possible flow disturbances, and the ROI was chosen such that this was in a straight part of the artery. This is referred to as the "optimal ROI." From these ROIs, 3 AIFs were created based on the magnitude of the signal (AIF_{MAGN}), phase (AIF_{PHASE}), and complex signal ($AIF_{COMPLEX}$). AIFs were first determined for the left and right artery separately and then averaged. We applied a hematocrit (Hct) correction of 1.18, based on an Hct of 0.38 and a small-to-large vessel ratio (r) of 0.7, to account for the volume of red blood cells in capillary blood,[22] using the relation[23] $(1 - rHct)/(1 - Hct)$. Averaged AIFs were fitted with a Gaussian and an exponential function modulated with a sigmoid function following the method of Parker et al.[11] From these fitted AIFs, the following parameters were extracted to characterize the curves: peak height, full width at half maximum (FWHM), the AUC, concentration of CA at 180 seconds (CI_{180}) as a measure for the height of the tail, and the standard deviation, describing the amount of noise in the tail, is calculated over a window from 160 to 200 seconds in the tail (std_{tail}).

To further investigate the sensitivity of the 3 methods to the location of ROIs in the craniocaudal direction, we performed an additional analysis for the data of the first MRI exam in a subgroup of 4 patients. Three AIFs were extracted

TABLE 1 Acquisition parameters of the DCE sequence, T2-weighted, and DWI sequence.

	Parameter	System I	System II	System III
	No. of patients	12	3	7
	System	Philips 3T Achieva	Philips 3T Achieva dStream	Philips 3T Ingenia
	Coil	Cardiac and endorectal	Anterior-posterior coil	Anterior-posterior coil
DCE	FOV (mm³)	360 × 518.4 × 60	360 × 517 × 60	262 × 262 × 60
	Acquired voxel size (mm³)	1.8 × 1.8 × 6	2.3 × 2.3 × 6	2 × 2 × 6
	Reconstructed voxel size (mm³)	1.2 × 1.2 × 3	1.4 × 1.4 × 3	1.2 × 1.2 × 3
	TR/TE (ms)	4/1.9	5/1.9	4/1.9
	Flip angle	20	20	13
	Parallel imaging factor	4	4	4
	Dynamic scan time (s)	2.6	2.9	2.5
	Total scan time (s)	300	300	300
	Injection rate (mL/s)	3	3	2
T2-weighted	FOV (mm³)	200 × 282 × 75	140 × 140 × 75	240 × 240 × 66
	Voxel size (mm³)	0.4 × 0.4 × 3	0.4 × 0.4 × 3	0.4 × 0.4 × 3
	TR/TE (ms)	Range 2500 to 5000/120	Range 2500 to 5000/120	Range 2500 to 5000/95
DWI	FOV (mm³)	160 × 160 × 83	180 × 180 × 60	262 × 262 × 66
	Voxel size (mm³)	1.1 × 1.1 × 3	1.0 × 1.0 × 3	1.4 × 1.4 × 3
	TR/TE (ms)	3500/59	3500/59	3500/65
	b-values (averages)	0 (1), 200 (4), 600 (4), 1000 (8)	0 (1), 200 (4), 600 (4), 1000 (8)	0 (5), 200 (5), 500 (5), 1000 (5)

in the cranial, medial, and caudal part of the femoral artery. $AIF_{CRANIAL}$ was defined as the average AIF extracted from the top 7 slices, including the first 3 cranial slices. AIF_{MEDIAL} was the averaged AIF in the ROI of the next 7 slices, and AIF_{CAUDAL} was the average AIF of the last 6 slices, including the last 3 caudal slices.

2.3.1 | Magnitude AIF

Magnitude AIF (AIF_{MAGN}) was determined by converting the magnitude of the signal to the concentration of CA using Schabel's method[14,24] (Equation 1):

$$|S| = \rho_{eff} \frac{\sin(\alpha)\left(1 - e^{-\frac{TR}{T_1(C)}}\right)}{1 - \cos(\alpha)\, e^{-\frac{TR}{T_1(C)}}} \tag{1}$$

with $|S|$ the magnitude of the signal, ρ_{eff} the spin density including system gain contributions, TR the repetition time, and α the flip angle. The flip angle was corrected for B_1-field inhomogeneity using the B_1 map. The dependency of T_1 on C (the concentration time curve [CTC]) is given by[25] (Equation 2):

$$\frac{1}{T_1(C)} = \frac{1}{T_{10}} + r_1 C \tag{2}$$

with r_1 the longitudinal CA relaxivity (3.5 mM^{-1}s^{-1} for gadoteric acid at 3T[26]) and T_{10} the precontrast T_1 value, which was fixed at 1932 ms.[27] For the relative signal enhancement, the spin density ρ_{eff} from Equation 1 drops out, resulting in (Equation 3):

$$\frac{|S| - |S_0|}{|S_0|} = \frac{\left(e^{-\frac{TR}{T_1(C)}} - 1\right)\left(\cos(\alpha)\, e^{-\frac{TR}{T_{10}(C)}} - 1\right)}{\left(e^{-\frac{TR}{T_{10}(C)}} - 1\right)\left(\cos(\alpha)\, e^{-\frac{TR}{T_1(C)}} - 1\right)} - 1 \tag{3}$$

with $|S_0|$ the average signal before contrast injection determined from the first 10 dynamic scans. This was solved by linear regression in Matlab (The MathWorks, Inc., Natick, MA) and in-house–built software, using the linear algebra package LAPACK.[28]

2.3.2 | Phase AIF

Phase AIF (AIF_{PHASE}) was calculated from the phase signal $\Delta\varphi$ using the method described by Akbudak et al.[29] The dependence of CA concentration on the phase signal is described by (Equation 4):

$$\Delta\varphi = \gamma \frac{\Delta \boldsymbol{B} \cdot \boldsymbol{H_o}}{\|\boldsymbol{H_0}\|} TE = \omega_0 \cdot \chi_M \cdot F \cdot C \cdot TE \tag{4}$$

with $\Delta\varphi = \varphi(C) - \varphi_0$, φ_0 the precontrast phase before CA injection, γ gyromagnetic ratio, $\Delta \boldsymbol{B}$ the change of the magnetic induction vector, $\boldsymbol{H}_0$ the static external magnetic field vector, ω_0 the resonance frequency, χ_M the molar susceptibility of the CA, and the geometric factor F given by (Equation 5):

$$F = \frac{1}{3} - \frac{1}{2}\sin^2\theta \tag{5}$$

where θ is the angle of the artery relative to the main magnetic field.

To correct for possible phase drift, an additional ROI was delineated close to the artery in fatty tissue, in such a way that ghosting or small vessels could not influence the signal.[15] This reference signal was smoothed with a Butterworth filter, using a cut-off frequency of 0.05 Hz and subsequently subtracted from the AIF_{PHASE}.

2.3.3 | Complex AIF

To determine the complex AIF ($AIF_{COMPLEX}$), the signal models to calculate the AIF from the magnitude and phase were combined into Equation 6:

$$S = \tilde{\rho}_{eff} \frac{\sin(\alpha)\left(1 - e^{-\frac{TR}{T_1(C)}}\right)}{1 - \cos(\alpha)\, e^{-\frac{TR}{T_1(C)}}} \cdot e^{\frac{-TE}{T_{2*}(C)}} \cdot e^{-i\Delta\varphi(C)} \tag{6}$$

For the T_1 and T_2^* of blood, a literature value of 1932 and 275 ms was chosen,[27] consistent with Simonis et al.[20] $\tilde{\rho}_{eff}$ was defined as a complex number, with $\tilde{\rho}_{eff} = \rho_{eff} \cdot e^{-i\Delta\varphi_0}$. The $AIF_{COMPLEX}$ concentration was determined with a variable projection algorithm VAPRO,[30] which is a weighted least square fitting procedure. The influence of phase drift[31] effects was reduced by lowering the weights of the cluster of points in the tail of the AIF, as described by Simonis et al.[20]

2.4 | Image processing

Registration between the images of the 2 exams was necessary to be able to compare the TK results of the 2 DCE-MRI scans. We used the transversal T2-weighted scans for intersession registration because it provides the anatomical detail necessary for accurate registration. First, a local rigid registration of the volume around the prostate was performed. Next, a deformable b-spline registration was applied.[32] The resulting deformation was subsequently applied to the T1 map, the B_1 map, and the DCE-MRI scan. However, before doing this, we visually checked whether there was intrasession displacement between the T2-weigthed and DCE-MRI scan. If this was the case, additional rigid registration was performed between the T2-weighted scan and the DCE-MRI scan.

In 2 patients, severe motion was visible during 1 DCE-MRI scan attributed to variations in rectum filling. For 1 patient, this was corrected by rigid registration of each time point to the last. For the other patient, this was corrected by removing the last 30 time points from the series. Further analyses were performed on these motion-corrected DCE-MRI scans.

For TK analysis, ROIs were defined in the healthy peripheral zone and suspected tumor tissue on the transversal T2-weigthed image of the second exam and copied to the first exam. This was based on mp-MRI data according the PI-RADS v2 criteria,[33] using the T2-weighted images, DWI with the apparent diffusion coefficient maps based on b-values of 200 and 1000, and the DCE-MRI scan. As recommended by PI-RADS v2, the DCE-MRI was only used to localize the cancer in those cases where the T2-weighting and DWI were inconclusive. They were not used to delineate the ROI. The ROIs of tumor and healthy peripheral zone were visually verified with corresponding hematoxylin and eosin–stained pathology slices. Postbiopsy hemorrhages were excluded from the delineations.

2.5 | Tracer kinetic analysis

Median signal intensities for each tumor and healthy ROI of the DCE-MRI scans were converted to CTCs using Equation 1. The precontrast T1 values were estimated for each ROI from the variable flip angle series with a nonlinear least squares fitting procedure.[34,35] The standard Tofts model[3] was applied to the CTCs, resulting in the volume transfer constant (K^{trans}) and the rate constant ($k_{ep} = K^{trans} / v_e$), with v_e referring to the extracellular extravascular space volume fraction. For this study, we only reported K^{trans} and k_{ep}, because v_e is directly related to K^{trans} and k_{ep}. We used an implementation similar to Murase et al.[36] This implementation assumes the same bolus arrival time for AIF and CTCs. So, before Tofts analysis, we shifted the AIFs and CTCs by estimating the delay using a regression model as proposed by Cheong et al.[37] A linear-linear piece-wise continuous function was fitted to the first 25 points of the CTC. It consisted of a straight line with slope 0 to fit the baseline part and a line with a slope >0 to fit the rising part of the CTC. The time point where these 2 lines intersect was taken as the bolus arrival time. To obtain the most accurate estimation of the bolus arrival time, the Tofts model was applied for 4 delay time points around the estimated bolus arrival time (–2 to +2 times the dynamic scan time in seconds). For each of these points, the χ^2 of the Tofts model curve was determined. The result with minimum χ^2 was chosen.

2.6 | Statistical Analysis

The curve characteristics of the AIF (i.e., peak height, FWHM, AUC, CI_{180}, and and std_{tail}) were compared between the 2 exams for each of the different AIF methods, using a Kruskal-Wallis nonparametric comparison test with Tukey-Kramer correction for multiple testing. Repeatability of the AIF curve characteristics was characterized with the within-subject coefficient of variation (wCV)[38] (Equation 7):

$$wCV = \sqrt{\frac{1}{n} \sum_{k=1}^{n} \frac{\left(Y_{1k} - Y_{2k}\right)^2 / 2}{\left(\left(Y_{1k} + Y_{2k}\right) / 2\right)^2}} \quad (7)$$

with n the number of patients and Y_{1k} 1 of the AIF curve characteristics of exam 1 and Y_{2k} 1 of the curve characteristics of exam 2. In case the standard deviation was dependent on the mean the results were first log transformed and the wCV was calculated as described by Bland and Altman.[39] The 95% confidence interval (CI) is determined as within-subject coefficient of variation (wCV) $\pm$ 1.96 $\times$ SE, with SE the standard error.

The variation attributed to the location was investigated by calculating the wCV (95% CI) between the AIFs determined from the left and right arteries where Y_{1k} in Equation 7 is 1 of the curve characteristics of the left artery and Y_{2k} 1 of the curve characteristics of the right artery. In addition, the wCV (95% CI) was calculated for the curve characteristics of either $AIF_{CRANIAL}$, AIF_{MEDIAL}, or AIF_{CAUDAL}, as Y_{1k}, compared to the AIF curve characteristics from the optimal ROI, as Y_{2k}.

To investigate differences in TK parameters (K^{trans} and k_{ep}) between tumor and healthy tissue per method (magnitude, phase, or complex), a nonparametric paired Wilcoxon signed-rank test was performed using the data of both exams. A post-hoc Tukey-Kramer multiple comparison test was applied to determine which method resulted in significantly different TK parameter values between the methods. To investigate repeatability between methods, the wCV (95% CI) between the 2 exams was calculated for healthy and tumor TK parameters combined. For all statistical tests, a P value <0.05 was considered statistically significant.

3 | RESULTS

3.1 | Patients

For 18 of the 22 patients, DCE-MRI data at 2 time points were available. Data of 2 patients had to be excluded because the second DCE-MRI exam was interrupted by the patient. For another patient, DCE-MRI data could not be used because of severe fold-over artifacts. The fourth patient was removed from the analysis because biopsies were taken between the first and second MRI.

For 2 patients, the AIF analysis and TK analysis was performed without a B_1 correction because of insufficient quality of the B_1 map. For the AIF analysis, there was 1

patient for whom the left artery was too curved to be able to find the artery angle as required for AIF_{PHASE}. Therefore, the AIF was only based on the right artery, and this patient was not used in the comparison of left and right arteries. For the TK analysis, in 2 patients, only ROIs with healthy tissue were used because no tumor tissue was visible on MRI. For another patient, none of the ROIs could be delineated because hemorrhage was present in the entire peripheral zone. For 1 patient, no pathology was available to validate the delineations. To summarize, the data of 18 patients were used for AIF analysis, whereas the data of 16 patients were used for TK analysis.

3.2 | AIF curve characteristics per method

Figure 1 shows 3 examples of the AIFs extracted from magnitude, phase, and complex signal. Curve characteristics of all patients are summarized in Table 2. For AIF_{MAGN}, peak height, FWHM, and AUC were significantly different in comparison to the other 2 methods ($P < 0.001$). Between AIF_{PHASE} and $AIF_{COMPLEX}$, there was no significant difference for peak height, FWHM, and AUC. The CI_{180} of $AIF_{COMPLEX}$ was significantly lower than for AIF_{PHASE} ($P < 0.0001$), but higher than of AIF_{MAGN} ($P < 0.0001$). The std_{tail} of $AIF_{COMPLEX}$ was significantly lower than for AIF_{PHASE} ($P < 0.0001$), but higher than for AIF_{MAGN} ($P < 0.0001$).

wCV values between the 2 exams are also shown in Table 2. Peak height of $AIF_{COMPLEX}$ had a lower wCV in comparison to that of AIF_{MAGN} and AIF_{PHASE} (Table 2), indicating a higher repeatability. wCV for FWHM was comparable between AIF_{PHASE} and $AIF_{COMPLEX}$. For the other curve characteristics, wCV values were similar between the 3 AIF methods, although AIF_{MAGN} had a higher repeatability for the curve characteristics describing the behavior of the tail (CI_{180} and std_{tail}).

Between the left and right AIFs, we observed a peak height ratio (left AIF/right AIF) for both AIF_{PHASE} and $AIF_{COMPLEX}$ of 1.0. For AIF_{MAGN}, this was 1.4, reflected in a higher wCV for peak height for AIF_{MAGN} compared to AIF_{PHASE} and $AIF_{COMPLEX}$ (Table 3). Without a B_1 correction, the peak height ratio for AIF_{MAGN} increased to 1.5, whereas the wCV increased from 15% to 20%.

We observed in 4 patients that the peak height was determined more consistently in the cranial, medial, and caudal part of the artery when the complex method was applied as compared to phase and amplitude. The relative standard deviation of the peak height determined in the 3 sections was approximately 50% for the magnitude, 25% for the phase, and 20% for the complex method.

3.3 | Tracer kinetic analysis

Figure 2 shows an example of the fits of the Tofts model for healthy and tumor tissue using each of the 3 AIFs. The K^{trans} values obtained for all patients for each exam are shown in Table 4. With all 3 types of AIF, we found significantly higher K^{trans} values in tumor compared to healthy tissue ($P < 0.001$). However, the K^{trans} values obtained with AIF_{MAGN} were approximately 6 times higher than obtained with AIF_{PHASE} or $AIF_{COMPLEX}$. For k_{ep}, we also found significant differences between tumor and healthy tissue.

Figure 3 shows Bland-Altman plots of K^{trans} and k_{ep} of repeated measurements using either 1 of the AIFs as input. This figure shows that variation in K^{trans} and k_{ep} is lower when AIF_{PHASE} and $AIF_{COMPLEX}$ are being used. The wCV calculated across all patients is shown in Figure 4, including the 95% CI. The wCV for K^{trans} obtained with AIF_{MAGN} was significantly larger than for the other 2 methods ($P = 0.0024$ and <0.001 for AIF_{PHASE} and $AIF_{COMPLEX}$, respectively); however, for k_{ep}, the wCVs were not significantly larger ($P = 0.45$ and 0.57 for AIF_{PHASE} and $AIF_{COMPLEX}$, respectively).
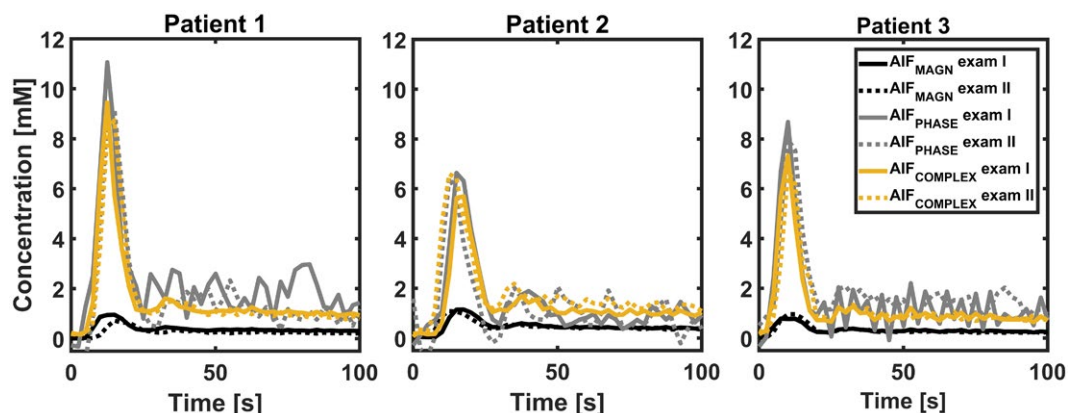

FIGURE 1 Examples of AIF_{MAGN}, AIF_{PHASE}, and $AIF_{COMPLEX}$ for 3 patients. The results for both exams are shown (exam 1 solid line, exam 2 dotted line). Only the first 100 seconds are shown to illustrate the differences in the peak of the AIF

TABLE 2 Median, range, and wCV with 95% CI of the AIF curve characteristics between the 2 consecutive exams

	Magnitude			Phase			Complex		
	Median (range)	wCV	(95% CI)	Median (range)	wCV	(95% CI)	Median (range)	wCV	(95% CI)
Peak height [mM]	0.8 (0.2–2.7)	12%	(8–17%)	8.3 (4.3–17.8)	12%	(8–16%)	7.3 (3.9–10.0)	7%	(5–9%)
FWHM [s]	15.2 (7.3–87.9)	12%	(8–16%)	9.2 (5.6–17.9)	7%	(5–9%)	9.5 (5.0–16.3)	8%	(5–10%)
AUC [mM * s]	71 (25–204)	12%	(8–16%)	479 (206–1080)	13%	(9–18%)	312 (206–754)	13%	(9–18%)
CI_{180}	0.2 (0.1–0.6)	12%	(8–16%)	1.4 (0.4–3.1)	15%	(10–20%)	0.8 (0.5–2.3)	18%	(12–23%)
std tail [mM]	0.0 (0.0–0.0)	9%	(6–12%)	0.4 (0.3–0.7)	12%	(8–16%)	0.1 (0.0–0.3)	14%	(9–18%)

Between the wCV obtained from phase and complex, we found no significant difference.

4 | DISCUSSION AND CONCLUSION

The aim of this study was to investigate repeatability of the AIF extracted from the complex signal compared to AIFs extracted from magnitude or phase signal and the effect on repeatability of the TK parameters. For this, we used test-retest DCE-MRI data of patients with prostate cancer and showed that repeatability for the TK parameters was higher when $AIF_{COMPLEX}$ was used.

For the AIF itself, we observed that the peak of $AIF_{COMPLEX}$ was similar to the peak of AIF_{PHASE} and that the tail of $AIF_{COMPLEX}$ was similar to AIF_{MAGN} with less noise than observed in the tail of AIF_{PHASE}. This illustrates that by using the complex signal, the advantageous properties of the magnitude and phase signal are being combined. This follows the findings of Simonis et al,[20] where they showed that the correlation between AIFs extracted from MRI and CT was higher when the complex signal was being used. However, in our data, less phase drift was observed, which could explain why AIF_{PHASE} and $AIF_{COMPLEX}$ were more similar for many characteristics compared to their results. Given that the presence of phase drift may vary between MRI scanners, in particular from different vendors, it makes sense to take this into account. In our sequences, the flip angle was relatively low, to allow a short dynamic scan time within SAR limitations. This may explain why the peak height determined from AIF_{MAGN} in our study is low. At 1.5T and with a larger flip angle, a short echo time, and a larger FOV in feet-head direction, most of the limitations of AIF_{MAGN} can be overcome.[14,40,41] However, this comes at the cost of a lower spatial or temporal resolution. In addition, imperfect spoiling can affect the peak height of the AIF.[42,43] Patients were scanned on 3 different systems, with different settings (flip angle, temporal resolution, and TE). In this study, we illustrate that even with a less-optimal flip angle and shorter TE, the repeatability of the peak estimation will be improved when an AIF is extracted from the complex signal.

The $AIF_{COMPLEX}$ and AIF_{PHASE} were less affected by the location of the ROIs than AIF_{MAGN}. Physiologically, we would not expect differences for AIFs from left or right artery. For AIF_{PHASE} and $AIF_{COMPLEX}$, the wCV was indeed small between left and right. However, for AIF_{MAGN}, we observed larger differences. The B_1 correction that was applied seemed relatively ineffective given that with or without B_1 correction, the left/right artery ratio for peak height was approximately the same (1.4–1.5). We also compared AIFs derived from cranial, medial, and caudal locations in the arteries. The lowest repeatability was observed with AIF_{MAGN}

TABLE 3 wCV between left and right AIFs, per method (magnitude, phase, and complex signal), with 95% CI for all curve characteristics

N = 18	Magnitude		Phase		Complex	
	wCV	(95% CI)	wCV	(95% CI)	wCV	(95% CI)
Peak height [mM]	15%	(10–20%)	4%	(3–6%)	4%	(3–6%)
FWHM [s]	20%	(14–27%)	3%	(2–4%)	9%	(6–13%)
AUC_{300} [mM * s]	8%	(6–11%)	11%	(7–15%)	19%	(12–25%)
CI_{180}	7%	(5–10%)	14%	(9–18%)	29%	(20–39%)
std tail [mM]	10%	(7–13%)	12%	(8–16%)	25%	(17–34%)
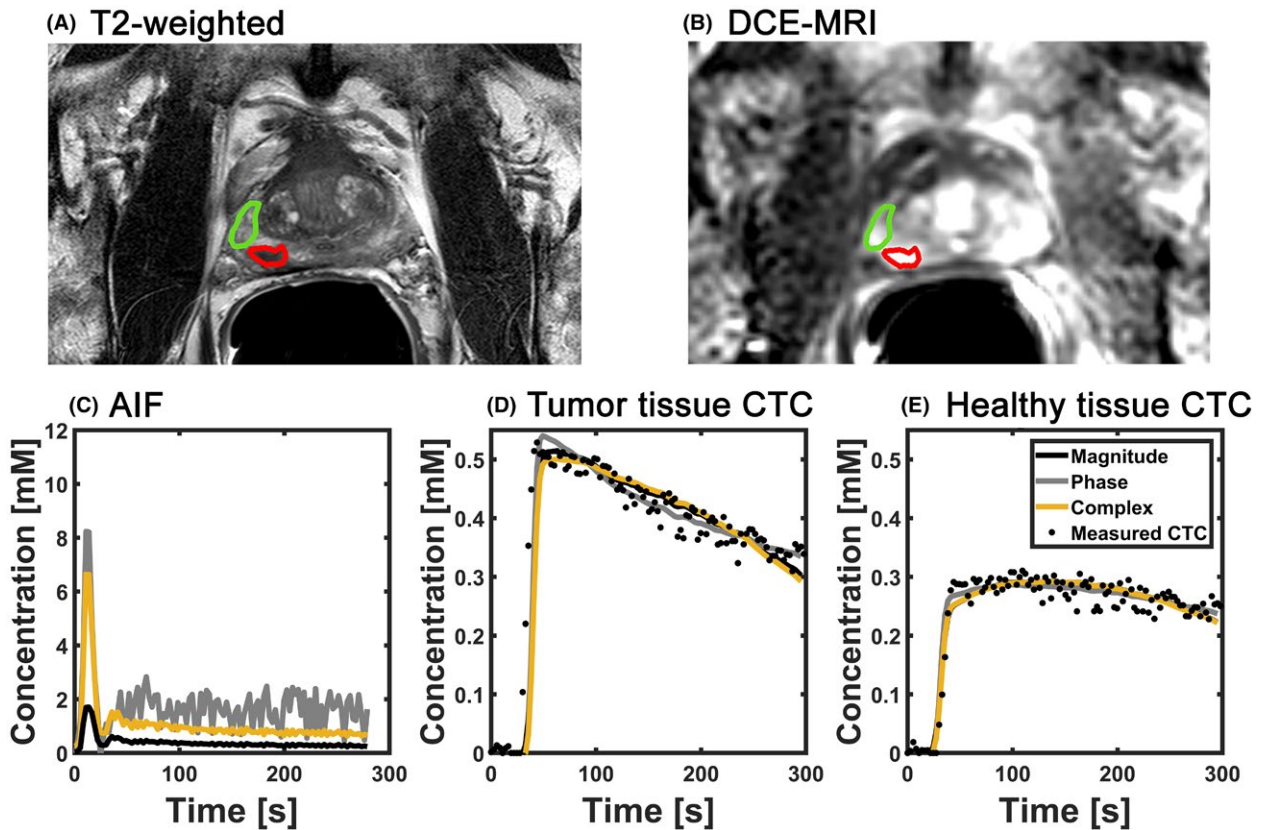
FIGURE 2 Example showing the effect of different types of AIFs used for TK analysis. The T2-weighted (a) and DCE-MRI magnitude scan at the 27th dynamic scan (b) are shown including delineations of tumor (red) and healthy peripheral zone (green). (c) The 3 types of AIFs (AIF_{MAGN}, AIF_{PHASE}, and $AIF_{COMPLEX}$). (d,e) CTCs for tumor and healthy tissue including the Tofts fits with each of the 3 AIFs

for cranial ROIs. This can be attributed to the inflow artifacts of the magnitude signal. For caudal ROIs, repeatability increased and came to be in the same range as AIF_{PHASE} and $AIF_{COMPLEX}$. Similar observations have been made by Cron et al[44] for a comparison between AIF_{MAGN} and AIF_{PHASE}.

K^{trans} and k_{ep} values for healthy and tumor tissues were different with all types of AIFs. In particular, K^{trans} values were approximately 6-fold higher with AIF_{MAGN} compared to those estimated from AIF_{PHASE} or $AIF_{COMPLEX}$, which is a result of the low peak height of AIF_{MAGN}. As shown earlier,[4,20] use of AIF_{PHASE} or $AIF_{COMPLEX}$ show a good agreement with the AIF as obtained from DCE-CT experiments. Simonis et al showed the highest correlation between the

AIFs obtained from DCE-MRI and DCE-CT when the complex AIF was used in comparison to AIFs from magnitude or phase signal.[20] We found that the repeatability of K^{trans} values was better with $AIF_{COMPLEX}$ compared to AIF_{MAGN} or AIF_{PHASE}, whereas for k_{ep} the differences were smaller. This improved repeatability could be related to the improved repeatability of the peak height, given that several simulation studies have shown that the characteristics of the peak have the largest influence on the TK parameters.[9,45] The wCV of the complex method to determine the tail of the AIF is higher than for the magnitude. The method to fit the tail of the AIF from the complex signal seems quite sensitive to noise on the magnitude and phase. This could

be improved by changing the weights for the fitting procedure in the complex plane for $AIF_{COMPLEX}$; however, this might have an influence on the fitting quality of the peak height, resulting in changes of repeatability for estimating K^{trans}. Several studies have shown that the most sensitive parts of the AIF with respect to TK parameters, particularly K^{trans}, are the peak height, AUC, and FWHM.[9,45] For example, deviations in peak height and FWHM of 10% can lead to a difference up to 20% in K^{trans} value.[9,45] Variations in the tail height (described by CI_{180}) have a smaller influence on K^{trans} estimation (10% difference leads to 2% difference in K^{trans}).[45] In addition, as described by Lavini,[45] the variations in tail had a similar effect on v_e estimation, where

10% difference in AUC or tail height leads to less than 10% difference in v_e. Given that repeatability not only depends on the choice of AIF, but, for example, also on the model, field strength, acquisition protocol, and location of ROI, it is difficult to compare our wCV data directly to existing literature. However, in general, the reported wCV of K^{trans} in ROIs is higher than what we observed for K^{trans} obtained with $AIF_{COMPLEX}$ (range, 12.5–57%).[46-50] Rata et al[51] reported a lower wCV of 7.5% when using a population AIF in a group of patients with abdominal tumors. To improve the accuracy of TK estimation, the promising approach presented by Brynolfsson et al[52] could be used, where they showed with simulated data that the concentration values

TABLE 4 Results of TKA parameters per exam for healthy and tumor ROIs for the 3 different methods

| K^{trans}		Exam 1 median (range) min^{-1}		Exam 2 median (range) min^{-1}	
Magnitude	Healthy	0.81	(0.35–4.10)	0.92	(0.30–4.87)
	Tumor	1.97	(0.43–29.2)	2.14	(0.74–10.7)
Phase	Healthy	0.13	(0.04–0.28)	0.11	(0.07–0.26)
	Tumor	0.30	(0.07–0.99)	0.31	(0.08–0.51)
Complex	Healthy	0.13	(0.07–0.33)	0.12	(0.07–0.32)
	Tumor	0.28	(0.08–1.07)	0.32	(0.14–0.69)
k_{ep}					
Magnitude	Healthy	0.83	(0.22–2.20)	0.76	(0.35–2.44)
	Tumor	1.53	(0.36–11.66)	1.25	(0.65–8.68)
Phase	Healthy	0.75	(0.19–1.37)	0.67	(0.30–0.98)
	Tumor	1.42	(0.51–3.55)	1.05	(0.43–3.64)
Complex	Healthy	0.50	(0.23–0.99)	0.52	(0.16–1.01)
	Tumor	0.85	(0.22–1.62)	0.86	(0.28–1.60)
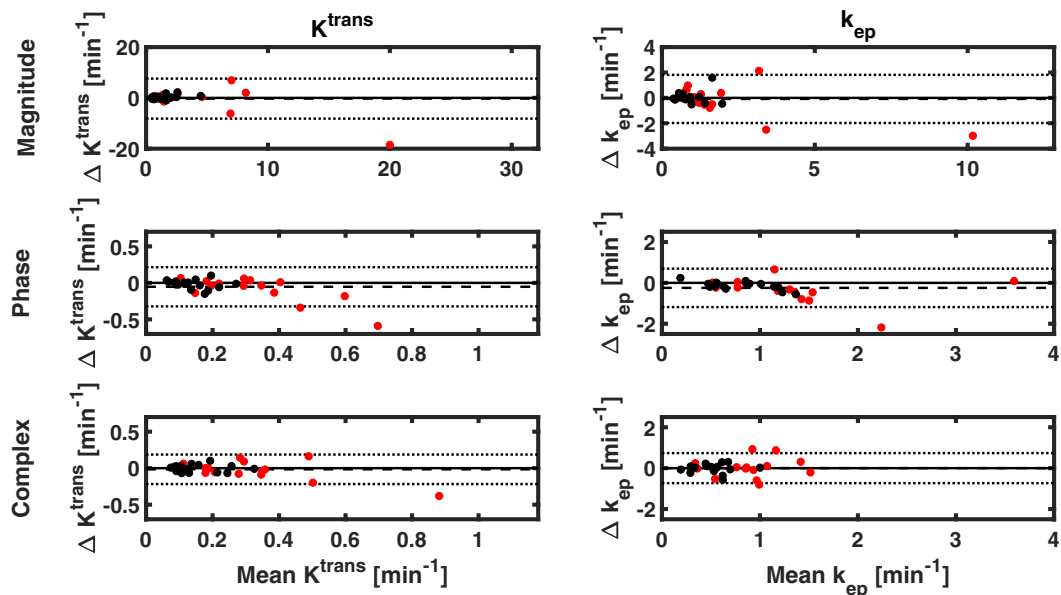
FIGURE 3 Bland-Altman plot for K^{trans} and k_{ep} for the 3 AIF methods. Dashed lines represent the bias, dotted lines the 95% confidence interval. Black dots represent results from healthy tissue, whereas red dots represent tumor tissue
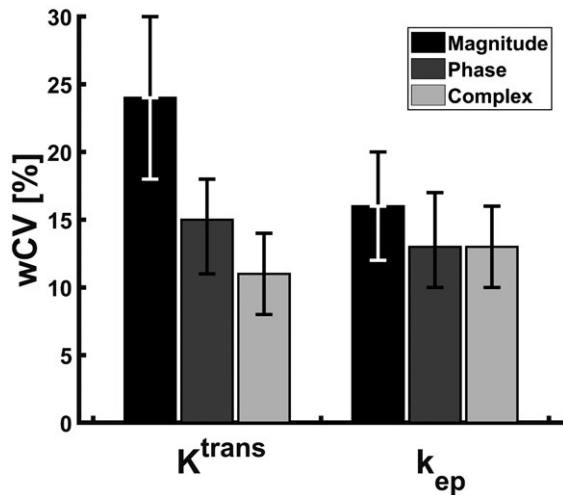
FIGURE 4 Bar plot of wCV values for K^{trans} and k_{ep} for the 3 AIF methods including 95% CI bars

in tissue were also more accurately determined when the complex data are used instead of the magnitude data alone.

A limitation of this study was that the CA dose was not scaled according to patient weight. This could explain the interpatient variability as reflected in the ranges of the AIF characteristics reported in Table 2. However, all AIF curve characteristics and TK parameters were compared pairwise, and therefore the repeatability results were not influenced by varying CA dose between patients. Another reason for the interpatient variability could be the Hct correction, which we based on literature values instead of individual patient measurements. Just et al[53] showed that a difference of 10% in Hct value can lead to underestimation in K^{trans} and especially in k_{ep} up to 60%.

In conclusion, when the complex MRI signal is being used to derive an AIF, repeatability of the peak is improved compared to an AIF estimated from either the magnitude or phase signal. Furthermore, the noise in the tail, as represented by std tail, was less in the AIF_{COMPEX} than in the AIF_{PHASE}, however, with a worse relative repeatability. In addition, it was shown that the complex AIF is less sensitive to the spatial location of the ROIs. As a consequence, repeatability of K^{trans} and k_{ep} is improved when an AIF based on either phase or complex signal is used, compared to a magnitude-based AIF.

ACKNOWLEDGMENT

ORCID

Edzo M.E. Klawer https://orcid.org/0000-0001-9882-2149

Petra J. van Houdt https://orcid.org/0000-0001-7431-8386

Frank F.J. Simonis https://orcid.org/0000-0002-0734-1778

Cornelis A.T. van den Berg https://orcid.org/0000-0002-5565-6889

Uulke A. van der Heide https://orcid.org/0000-0002-4146-6419

REFERENCES

1. Padhani AR, Hayes C, Landau S, Leach MO. Reproducibility of quantitative dynamic MRI of normal human tissues. *NMR Biomed*. 2002;15:143–153.

2. Gribbestad I, Gjesdal K, Nilsen G, Lundgren S, Hjelstuen M, Jackson A. An introduction to dynamic contrast-enhanced MRI in oncology. In Jackson A, Buckley DL, Parker GJM, eds. *Dynamic Contrast-Enhanced Magnetic Resonance Imaging in Oncology*. Berlin; Heidelberg, Germany: Springer; 2005:3–22.

3. Tofts PS, Brix G, Buckley DL, et al. Estimating kinetic parameters from dynamic contrast-enhanced T(1)-weighted MRI of a diffusable tracer: standardized quantities and symbols. *J Magn Reson Imaging*. 1999;10:223–232.

4. Korporaal JG, Van Den Berg CA, Van Osch MJ, Groenendaal G, Van Vulpen M, Van Der Heide UA. Phase-based arterial input function measurements in the femoral arteries for quantification of dynamic contrast-enhanced (DCE) MRI and comparison with DCE-CT. *Magn Reson Med*. 2011;66:1267–1274.

5. Heye T, Davenport MS, Horvath JJ, et al. Reproducibility of dynamic contrast-enhanced MR imaging. Part I. Perfusion characteristics in the female pelvis by using multiple computer-aided diagnosis perfusion analysis solutions. *Radiology*. 2013;266:801–811.

6. Ng CS, Raunig DL, Jackson EF, et al. Reproducibility of perfusion parameters in dynamic contrast-enhanced MRI of lung and liver tumors: effect on estimates of patient sample size in clinical trials and on individual patient responses. *AJR Am J Roentgenol*. 2010;194:W134–W140.

7. Duan C, Kallehauge JF, Bretthorst GL, Tanderup K, Ackerman JJ, Garbow JR. Are complex DCE-MRI models supported by clinical data? *Magn Reson Med*. 2017;77:1329–1339.

8. Cuenod CA, Balvay D. Perfusion and vascular permeability: basic concepts and measurement in DCE-CT and DCE-MRI. *Diagn Interv Imaging*. 2013;94:1187–1204.

9. Garpebring A, Brynolfsson P, Yu J, et al. Uncertainty estimation in dynamic contrast-enhanced MRI. *Magn Reson Med*. 2013;69:992–1002.

10. Buckley DL. Uncertainty in the analysis of tracer kinetics using dynamic contrast-enhanced T1-weighted MRI. *Magn Reson Med*. 2002;47:601–606.

11. Parker GJ, Roberts C, Macdonald A, et al. Experimentally-derived functional form for a population-averaged high-temporal-resolution arterial input function for dynamic contrast-enhanced MRI. *Magn Reson Med*. 2006;56:993–1000.

12. Port RE, Knopp MV, Brix G. Dynamic contrast-enhanced MRI using Gd-DTPA: interindividual variability of the arterial input

function and consequences for the assessment of kinetics in tumors. *Magn Reson Med*. 2001;1038:1030–1038.

13. Rijpkema M, Kaanders JH, Joosten FB, van der Kogel AJ, Heerschap A. Method for quantitative mapping of dynamic MRI contrast agent uptake in human tumors. *J Magn Reson Imaging*. 2001;14:457–463.

14. Schabel MC, Parker DL. Uncertainty and bias in contrast concentration measurements using spoiled gradient echo pulse sequences. *Phys Med Biol*. 2008;53:2345–2373.

15. Garpebring A, Wirestam R, Yu J, Asklund T, Karlsson M. Phase-based arterial input functions in humans applied to dynamic contrast-enhanced MRI: potential usefulness and limitations. *MAGMA*. 2011;24:233–245.

16. Cheng HL, Wright GA. Rapid high-resolutionT1 mapping by variable flip angles: Accurate and precise measurements in the presence of radiofrequency field inhomogeneity. *Magn Reson Med*. 2006;55:566–574.

17. Haacke EM, Brown RW, Thompson MR, Venkatesan R. *Magnetic Resonance Imaging: Physical Principles and Sequence Design*. New York: Wiley; 1999.

18. Van Osch MJ, Vonken EJ, Bakker CJ, Viergever MA. Correcting partial volume artifacts of the arterial input function in quantitative cerebral perfusion MRI. *Magn Reson Med*. 2001;45:477–485.

19. de Bruin PW, Reijnierse M, van Osch MJ. Partial volume correction of arterial input functions in T1-weighted dynamic contrast-enhanced MRI. In Proceedings of the 18th Annual Meeting of ISMRM, Stockholm, Sweden, 2010. p. 1.

20. Simonis FF, Sbrizzi A, Beld E, Lagendijk JJ, van den Berg CA. Improving the arterial input function in dynamic contrast enhanced MRI by fitting the signal in the complex plane. *Magn Reson Med*. 2016;76:1236–1245.

21. Yarnykh VL. Actual flip-angle imaging in the pulsed steady state: a method for rapid three-dimensional mapping of the transmitted radiofrequency field. *Magn Reson Med*. 2007;57:192–200.

22. Parker G, Buckley D. Tracer kinetic modelling for T1-weighted DCE-MRI. In Jackson A, Buckley DL, Parker GJ, eds. *Dynamic Contrast-Enhanced Magnetic Resonance Imaging in Oncology*. Heidelberg, Germany: Springer; 2005.

23. Henderson E, Milosevic MF, Haider MA, Yeung IW. Functional CT imaging of prostate cancer. *Phys Med Biol*. 2003;48:3085–3100.

24. Bernstein M, King K, Zhou X. *Handbook of MRI Pulse Sequences*, 1st ed. Amsterdam: Elsevier Academic; 2004.

25. Donahue KM, Weisskoff RM, Burstein D. Water diffusion and exchange as they influence contrast enhancement. *J Magn Reson Imaging*. 1997;7:102–110.

26. Rohrer M, Bauer H, Mintorovitch J, Requardt M, Weinmann HJ. Comparison of magnetic properties of MRI contrast media solutions at different magnetic field strengths. *Invest Radiol*. 2005;40:715–724.

27. Stanisz GJ, Odrobina EE, Pun J, et al. T1, T2 relaxation and magnetization transfer in tissue at 3T. *Magn Reson Med*. 2005;54:507–512.

28. Anderson E, Bai Z, Bischof C, et al. *LAPACK users' guide*. 3rd ed. Philadelphia, PA: Society for Industrial and Applied Mathematics

29. Akbudak E, Norberg RE, Conturo TE. Contrast-agent phase effects: an experimental system for analysis of susceptibility, concentration, and bolus input function kinetics. *Magn Reson Med*. 1997;38:990–1002.

30. Golub G, Pereyra V. Separable nonlinear least squares: the variable projection method and its applications. 1. Introduction. *Inverse Probl*. 2003;19:1–26.

31. Hijnen NM, Elevelt A, Pikkemaat J, Bos C, Bartels LW, Grüll H. The magnetic susceptibility effect of gadolinium-based contrast agents on PRFS-based MR thermometry during thermal interventions. *J Ther ultrasound*. 2013;1:8.

32. Mencarelli A, Van Kranen SR, Hamming-Vrieze O, et al. Deformable image registration for adaptive radiation therapy of head and neck cancer: accuracy and precision in the presence of tumor changes. *Int J Radiat Oncol Biol Phys*. 2014;90:680–687.

33. Barentsz JO, Richenberg J, Clements R, et al. ESUR prostate MR guidelines 2012. *Eur Radiol*. 2012;22:746–757.

34. Chang LC, Cheng GK, Basser PJ, Pierpaoli C. Linear least-squares method for unbiased estimation of T1 from SPGR signals. *Magn Reson Med*. 2008;60:496–501.

35. Deoni SCL, Rutt BK, Peters TM. Rapid combined T1 and T2 mapping using gradient recalled acquisition in the steady state. *Magn Reson Med*. 2003;49:515–526.

36. Murase K. Efficient method for calculating kinetic parameters using T1-weighted dynamic contrast-enhanced magnetic resonance imaging. *Magn Reson Med*. 2004;51:858–862.

37. Cheong LH, Koh TS, Hou Z. An automatic approach for estimating bolus arrival time in dynamic contrast MRI using piecewise continuous regression models. *Phys Med Biol*. 2003;48:83–88.

38. Bland JM, Altman DG. Statistical methods for assessing agreement between two methods of clinical measurement. *Lancet*. 1986;1:307–310.

39. Bland JM, Altman DG. Measurement error proportional to the mean. *BMJ*. 1996;313:106.

40. Sourbron S. Technical aspects of MR perfusion. *Eur J Radiol*. 2010;76:304–313.

41. De Naeyer D, Verhulst J, Ceelen W, Segers P, De Deene Y, Verdonck P. Flip angle optimization for dynamic contrast-enhanced MRI-studies with spoiled gradient echo pulse sequences. *Phys Med Biol*. 2011;56:5373–5395.

42. Garpebring A, Wirestam R, Östlund N, Karlsson M. Effects of inflow and radiofrequency spoiling on the arterial input function in dynamic contrast-enhanced MRI: a combined phantom and simulation study. *Magn Reson Med*. 2011;65:1670–1679.

43. Yarnykh VL. Optimal radiofrequency and gradient spoiling for improved accuracy of T1 and B1 measurements using fast steady-state techniques. *Magn Reson Med*. 2010;63:1610–1626.

44. Cron GO, Foottit C, Yankeelov TE, Avruch LI, Schweitzer ME, Cameron I. Arterial input functions determined from MR signal magnitude and phase for quantitative dynamic contrast-enhanced MRI in the human pelvis. *Magn Reson Med*. 2011;66:498–504.

45. Lavini C. Simulating the effect of input errors on the accuracy of Tofts' pharmacokinetic model parameters. *Magn Reson Imaging*. 2015;33:222–235.

46. Yang C, Karczmar GS, Medved M, Oto A, Zamora M, Stadler WM. Reproducibility assessment of a multiple reference tissue method for quantitative dynamic contrast enhanced-MRI analysis. *Magn Reson Med*. 2009;61:851–859.

47. Kershaw LE, Hutchinson CE, Buckley DL. Benign prostatic hyperplasia: Evaluation of T1, T2, and microvascular characteristics with T1-weighted dynamic contrast-enhanced MRI. *J Magn Reson Imaging*. 2009;29:641–648.

48. Ng CS, Wei W, Bankson JA, et al. Dependence of DCE-MRI biomarker values on analysis algorithm. *PLoS ONE*. 2015;10:e0130168.

49. Alonzi R, Taylor NJ, Stirling JJ, et al. Reproducibility and correlation between quantitative and semiquantitative dynamic and intrinsic susceptibility-weighted MRI parameters in the benign and malignant human prostate. *J Magn Reson Imaging*. 2010;32:155–164.

50. Jones KM, Pagel MD, Cárdenas-Rodríguez J. Linearization improves the repeatability of quantitative dynamic contrast-enhanced MRI. *Magn Reson Imaging*. 2018;47:16–24.

51. Rata M, Collins DJ, Darcy J, et al. Assessment of repeatability and treatment response in early phase clinical trials using DCE-MRI: comparison of parametric analysis using MR- and CT-derived arterial input functions. *Eur Radiol*. 2016;26:1991–1998.

52. Brynolfsson P, Yu J, Wirestam R, Karlsson M, Garpebring A. Combining phase and magnitude information for contrast agent quantification in dynamic contrast-enhanced MRI using statistical modeling. *Magn Reson Med*. 2015;74:1156–1164.

53. Just N, Koh DM, D'Arcy J, Collins DJ, Leach MO. Assessment of the effect of haematocrit-dependent arterial input functions on the accuracy of pharmacokinetic parameters in dynamic contrast-enhanced MRI. *NMR Biomed*. 2011;24:902–915.